

Mitigation of birefringence in cavity-based quantum networks using frequency-encoded photons

Chengxi Zhang,¹ Justin Phillips,^{1,2} Inder Monga,² Erhan Saglamyurek,^{1,2} Qiming Wu,^{1,2,*} and Hartmut Haefner^{1,2}

¹*Department of Physics, University of California, Berkeley, CA 94720, USA*

²*Lawrence Berkeley National Laboratory, Berkeley, CA 94720, USA*

(Dated: March 10, 2025)

Atom-cavity systems offer unique advantages for building large-scale distributed quantum computers by providing strong atom-photon coupling while allowing for high-fidelity local operations of atomic qubits. However, in prevalent schemes where the photonic state is encoded in polarization, cavity birefringence introduces an energy splitting of the cavity eigenmodes and alters the polarization states, thus limiting the fidelity of remote entanglement generation. To address this challenge, we propose a scheme that encodes the photonic qubit in the frequency degree-of-freedom. The scheme relies on resonant coupling of multiple transverse cavity modes to different atomic transitions that are well-separated in frequency. We numerically investigate the temporal properties of the photonic wavepacket, two-photon interference visibility, and atom-atom entanglement fidelity under various cavity polarization-mode splittings and find that our scheme is less affected by cavity birefringence. Finally, we propose practical implementations in two trapped ion systems, using the fine structure splitting in the metastable D state of $^{40}\text{Ca}^+$, and the hyperfine splitting in the ground state of $^{225}\text{Ra}^+$. Our study presents an alternative approach for cavity-based quantum networks that is less sensitive to birefringent effects, and is applicable to a variety of atomic and solid-state emitter-cavity interfaces.

I. INTRODUCTION

Atom- and ion-based quantum processors promise opportunities for large-scale, high-fidelity quantum computation, enhanced quantum sensing and metrology, quantum simulation of many-body physics and quantum chemistry problems [1–7]. However, scaling beyond thousands of qubits within a single processing unit (node) poses significant technical challenges [8, 9]. This limitation has driven the development of quantum networks [10, 11], that utilize photons to connect distant physical systems and enable distributed quantum computation [12–14]. For example, remote entanglement can be probabilistically established between distant nodes via quantum teleportation which relies on interference of two photons that are entangled with stationary atomic qubits in each node. [15, 16]. This approach overcomes some of the physical constraints of single-node processors and allows photonic-interconnected quantum systems to solve larger computational tasks [17–19].

The main challenge for remote entanglement generation (REG) is to improve the photon extraction efficiency while retaining high fidelity. In traditional free-space setups, the collection efficiency of spontaneously emitted photons is limited by the solid angle of the objective lenses [20–22]. In contrast, optical cavities offer the potential for higher collection efficiency by modifying the atomic spontaneous emission, such that photons preferentially decay into the cavity mode [23–25]. Despite their potential for enhanced efficiency, cavity-based quantum networks are particularly susceptible to errors

arising from photon distinguishability due to a number of factors, including spontaneous emission, cavity jittering, and cavity birefringence [26]. Notably, cavity birefringence presents a substantial challenge for the commonly used polarization encoding scheme. In particular, micro-cavity systems [27] are highly desirable because of the increased atom-cavity coupling [28, 29] but they are more prone to birefringence. Manufacturing imperfections and mechanical stress give rise to ellipticity of the cavity mirrors [30, 31] that splits the energies of the two polarization eigenmodes, causing a time-dependent oscillation of the polarization states. Furthermore, in long-distance fiber links, polarization drift and fluctuations introduce additional technical challenges for reliable polarization qubit measurements [22, 32], which is another undesirable feature of polarization encoding for robust quantum networks. The inherent susceptibility to birefringence together with the instability of polarization qubit measurements has stimulated the search for alternative encoding methods, including the time-bin scheme, which has already shown promise in terms of higher fidelities, easy implementation of quantum frequency conversion, and its insensitivity to polarization errors, albeit with typically lower entangling rates [33–36].

We propose an alternative approach to a cavity-based quantum network that utilizes frequency encoding of photonic qubits [37, 38]. This approach relies on matching the frequency difference between two selected atomic qubit transitions to an even multiple of the cavity’s free spectral range (FSR). In this way, both frequency qubit states can share the same polarization and resonate with the fundamental mode of the cavity. Furthermore, the atom can be located at the antinode position of the cavity center for both encoded frequencies with a maximal coupling strength.

* qiming.wu@berkeley.edu

Our analytical and numerical analysis confirms that frequency encoding can achieve a high-degree of indistinguishability between the photonic wavepackets that enhances two-photon interference visibility, and is expected to improve the fidelity of REG in the presence of birefringence. The residual errors arise primarily from the difference in birefringence of the two networking nodes considered and can be further reduced by tuning other cavity parameters to improve the temporal mode matching. Finally, we outline and simulate two feasible experimental implementations with realistic physical parameters: one using fine structure splitting in the metastable D state of $^{40}\text{Ca}^+$ and another using hyperfine splitting in the ground state of $^{225}\text{Ra}^+$, indicating the practical use of our scheme.

The paper is organized as follows: in Section II, we discuss the theoretical framework of atom-cavity quantum networks, including the use of two-photon interference for heralded entanglement and the sources of fidelity loss. We then introduce the frequency encoding scheme, detailing how it mitigates the errors from birefringence. Section III focuses on the analytical modeling and derivation of the methods used in our simulations. Section IV shows the numerical results, including the analysis of the photonic wavepacket, two-photon interference visibility, and the robustness of entanglement fidelity under various cavity parameters. In Section V, we explore the experimental feasibility of implementing frequency encoding with different atomic species. Section VI concludes with a summary and an outlook for future experimental realization.

II. FREQUENCY ENCODING IN ATOM-CAVITY SYSTEMS

In this section, we describe the basics of heralded entanglement in the context of performing two-photon interference. We also introduce the proposed frequency encoding scheme and discuss a few sources of fidelity loss.

A. Heralded entanglement based on two photon interference

We consider an atom-cavity system with energy levels shown in Fig. 1(a). At the beginning of each experimental cycle, the atom is initialized in the state $|i\rangle$. Then it simultaneously undergoes two cavity-assisted Raman transitions (CARTs) [39, 40] from $|i\rangle$ to qubit states $|\uparrow\rangle$ and $|\downarrow\rangle$, mediated by the excited state $|e\rangle$. Each transition is driven by an off-resonant laser (blue and red straight arrows), with the emitted photons coupled into cavity modes (blue and red curved arrows). The two resulting photonic states are required to have orthogonal characteristics, such as different polarizations, frequencies, or emission times, corresponding to different photonic qubit encoding schemes. If the strengths of

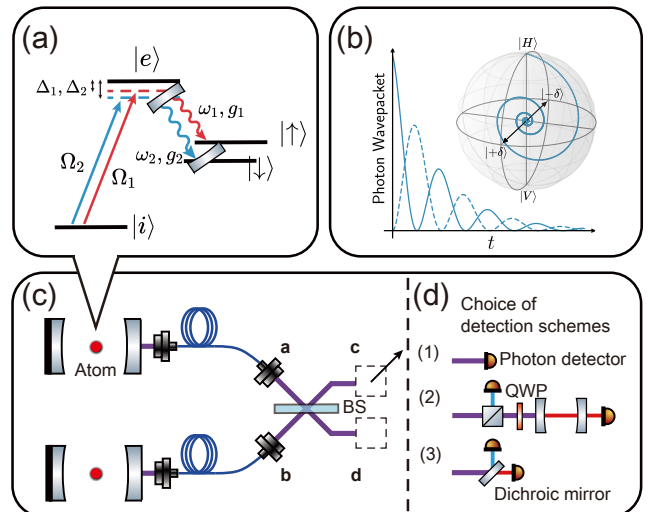


FIG. 1. Frequency-encoded quantum network. (a) Atomic energy level diagram. The atom is first prepared in the initial state $|i\rangle$ and undergoes two simultaneous cavity-assisted Raman transitions (red and blue). Population is coherently transferred from $|i\rangle$ to $|\uparrow\rangle$ and $|\downarrow\rangle$ via virtual coupling to an excited state $|e\rangle$, associated with photons of two distinct colors emitted into two cavity modes. Straight arrows denote the off-resonant laser drives and wavy arrows are photons mediated by atom-cavity coupling. This process entangles the atom's qubit state with the photonic qubit as $\frac{1}{\sqrt{2}}(|\uparrow\rangle|r\rangle + e^{i\theta}|\downarrow\rangle|b\rangle)$. (b) Polarization oscillation in a birefringent cavity. The solid ($|H\rangle$) and dashed ($|V\rangle$) curves represent the temporal probability density of photon state decomposition in the two polarization basis. The state evolution is also plotted on a Poincaré sphere, with the amplitude representing the probability to detect a photon at time t . (c) Photons from both nodes described in (a) are injected into a beam splitter to generate entanglement. Multiple measurement schemes of frequency-encoded photons can be applied at the output ports: (1) direct photon detection, (2) separation by a cavity with detection for each color, (3) separation by a dichroic mirror with detection for each color. The methods vary in efficiency and fidelity, allowing a trade-off between performance and experimental simplicity.

both Raman transitions are tuned to be identical, the atom-photon system ends up in a maximally entangled state $|\phi\rangle = \frac{1}{\sqrt{2}}(|\uparrow\rangle|0\rangle + e^{i\theta}|\downarrow\rangle|1\rangle)$, where the $|0\rangle, |1\rangle$ basis represents a general photonic qubit. Depending on the chosen encoding scheme, the basis can be defined as $|H\rangle, |V\rangle$ (for horizontally and vertically polarized photons); $|r\rangle, |b\rangle$ (for photons with lower and higher frequency); $|\text{early}\rangle, |\text{late}\rangle$ (for early or late emission), etc. The relative phase θ is determined by the relative laser phase in the bichromatic drive. Without loss of generality, we will default to frequency encoding, and denote the photonic qubit as $|r\rangle$ and $|b\rangle$ for the low- and high-frequency photon state, respectively.

After generating an atom-photon entangled state at

each node, the two photons are sent to the input ports \mathbf{a} and \mathbf{b} of a beam splitter for two-photon interference [41, 42]. The annihilation operators from each node a, b are transformed by the beam splitter according to the unitary operation

$$\begin{cases} a = \frac{1}{\sqrt{2}}c - \frac{1}{\sqrt{2}}d, \\ b = \frac{1}{\sqrt{2}}c + \frac{1}{\sqrt{2}}d. \end{cases} \quad (1)$$

Measurements are then performed at output ports \mathbf{c} and \mathbf{d} in the $|r\rangle, |b\rangle$ basis (Fig. 1(c)). Ideally, with photons from both nodes being perfectly indistinguishable, the state after the beam splitter transformation is given by:

$$\begin{aligned} |\Phi\rangle = & \frac{1}{4} \left[\sqrt{2} \left(|r_c r_c\rangle - |r_d r_d\rangle \right) |\uparrow\uparrow\rangle \right. \\ & + \sqrt{2} \left(|b_c b_c\rangle - |b_d b_d\rangle \right) |\downarrow\downarrow\rangle \\ & + |r_c b_c\rangle \left(|\uparrow\downarrow\rangle + |\downarrow\uparrow\rangle \right) - |r_d b_d\rangle \left(|\uparrow\downarrow\rangle + |\downarrow\uparrow\rangle \right) \\ & \left. + |r_c b_d\rangle \left(|\uparrow\downarrow\rangle - |\downarrow\uparrow\rangle \right) - |r_d b_c\rangle \left(|\uparrow\downarrow\rangle - |\downarrow\uparrow\rangle \right) \right], \end{aligned} \quad (2)$$

where the photonic qubit is denoted such that $|r_c r_c\rangle = c_r^\dagger c_r^\dagger |0\rangle$ represents the state causing two red photons to arrive at port \mathbf{c} . The equation shows a combination of all possible coincidence events and the corresponding atom-atom state after photon detection. For example, a successful detection of one red photon in port \mathbf{c} and one blue photon in port \mathbf{d} heralds the asymmetric Bell state $|\psi^-\rangle = (|\uparrow\downarrow\rangle - |\downarrow\uparrow\rangle)/\sqrt{2}$. The generation of such a maximally entangled state relies on the indistinguishability of photons from the two nodes: when we detect $|r_c b_d\rangle$ and the path information is erased, the atom-atom state collapses to a superposition of $|\downarrow\uparrow\rangle$ and $|\uparrow\downarrow\rangle$.

We note that in order to herald on both asymmetric Bell states $|\Psi^\pm\rangle$, the realization of the measurement depends on the chosen encoding scheme. For polarization-encoded photons, polarization beam splitters (PBS) can be used at output ports \mathbf{c} and \mathbf{d} , with two photon detectors after the output ports of each PBS. For frequency-encoded photons, a second cavity resonating with only one of the two frequencies can distinguish the frequency qubit, as shown in Fig. 1(d)(2). Also, a dichroic mirror (3) can be applied if the frequency difference is beyond a few THz. Directly detecting the photons that appears at both ports (1) without distinguishing their frequencies is also feasible [37]. This approach simplifies detection, but cannot herald $|\Psi^+\rangle$, reducing efficiency by 50% and possibly leading to additional fidelity loss with nonidentical photons due to anti-bunching effects [43].

B. Sources of fidelity loss

While Eq. 2 presents an ideal atom-atom entanglement result, in practice multiple factors can lead to imperfect fidelity. For instance, a difference in photonic wavepacket shape between the two nodes reduces the final fidelity because it introduces distinguishability. Such a difference could arise from the different parameter settings between nodes. The distinguishability of the two nodes from probabilistic events such as re-excitation errors (discussed in detail in Section III D), and technical noise such as cavity jitter [26], also contribute to reduced fidelity.

Mirror-induced birefringence is another important source of fidelity loss. Although cavity-based photon collection schemes may enhance collection efficiency, their mirrors often exhibit birefringence because of inherent ellipticity and mechanical stress, especially in microcavities. The mirror birefringence introduces an energy splitting to the non-degenerate modes of polarization. As a result, superpositions of the polarization eigenstates of photons in the cavity rotate as a function of time. Fig. 1(b) illustrates the evolution of a $|H\rangle$ photon emitted in a birefringent cavity with coupling parameters of $(\kappa, \gamma, \delta) = (0.01, 0, 0.05)g$. Spontaneous atomic decay γ is ignored and a small cavity decay κ is chosen here to illustrate the polarization oscillation in the cavity. Here, g represents the atom-cavity coupling rate and 2δ is the birefringent splitting. The cavity eigenmodes $|\pm\delta\rangle$ are set to $(|H\rangle \pm |V\rangle)/\sqrt{2}$, causing the $|H\rangle$ photon to undergo a rotation while its amplitude gradually decreases. The left side shows the oscillations in projection onto the horizontal and vertical polarization basis, while the right side shows the corresponding trajectory on the Poincaré sphere. This effect causes the entangled atom-photon state to be time-dependent. Consequently, the heralded atom-atom state will include extra unwanted components in $|\uparrow\uparrow\rangle$ and $|\downarrow\downarrow\rangle$ that depend on the detection, and more importantly, on the unknown emission times.

To address the birefringence effect, in addition to improving mirror manufacturing [31, 44], some pre- and post-herald correction methods have been proposed to compensate for such rotation by applying a time-dependent unitary transformation to the photonic or atomic qubit [45]. Here we propose frequency encoding as a robust alternative to mitigate the effect of birefringence on the fidelity. Although birefringence still induces polarization rotation, photons encoded with distinct frequencies can be distinguished during measurement. Thus, even if the photon has a time-varying polarization in the cavity, the frequency-dependent heralding procedure yields results that are uniquely correlated to the atom's decay path. With no misidentifications caused by the birefringence-induced polarization rotation, the error rate can be substantially reduced. While fidelity loss due to the distinguishability in the polarization degree-of-freedom may still be present, this effect may be suppressed by choosing the same polarization for both emission paths.

III. MODELS AND METHODS

This section provides a detailed derivation of the REG mechanism, with the fidelity-reducing error sources discussed in Section II B taken into account. The equations provided here will be used for the numerical simulations discussed in Section IV. In Section III A we discuss the atom-photon entanglement generation process, focusing on the system's pure and mixed evolution based on its Hamiltonian. Section III B and III C present the two-photon interference process and the resulting REG fidelity.

A. Atom-photon entanglement

During the generation of entangled atom-photon pairs, each node operates independently and simultaneously. We consider an atom going through two simultaneous cavity-assisted Raman transitions (CARTs), as shown in Fig. 1(a). Four levels are involved in the transition, where $|i\rangle$ is the initial state, $|e\rangle$ is the excited state and $|\uparrow\rangle$ and $|\downarrow\rangle$ are the qubit states. During each REG attempt, the atom is driven from $|i\rangle$ to qubit states $|\uparrow\rangle$ and $|\downarrow\rangle$ with equal strength, through an off-resonant bichromatic laser coupling $|i\rangle$ and $|e\rangle$, accompanied by emission of cavity photons. In frequency encoding, the emitted photons should share the same polarization to ensure that they evolve identically under birefringence. Without loss of generality, we assume that the photons are horizontally polarized.

The Hilbert space of the atom-cavity system is described by the tensor product of the atomic and photonic state. Here, only the states involved in the Raman pro-

cess are considered: $|i\rangle$, $|e\rangle$, $|\uparrow\rangle|rH\rangle$, $|\uparrow\rangle|rV\rangle$, $|\downarrow\rangle|bH\rangle$, $|\downarrow\rangle|bV\rangle$, where $|r\rangle$ and $|b\rangle$ denote the red and blue photon frequency states, and $|H\rangle$ and $|V\rangle$ represent the horizontal and vertical polarization. Evolution of the system in the CART follows the Lindblad equation:

$$\dot{\rho} = -\frac{i}{\hbar} (H\rho - \rho H^\dagger) + \sum_j \left(L_j \rho L_j^\dagger - \frac{1}{2} \{L_j^\dagger L_j, \rho\} \right), \quad (3)$$

where the full Hamiltonian can be written as:

$$H = H_0 + H_L + H_{\text{Cav}} + H_{\text{Bire}} + H_\kappa + H_\gamma. \quad (4)$$

Here, H_0 represents the bare atomic energy levels, H_L denotes the atom-laser interaction and H_{Cav} denotes the atom-cavity interaction. The birefringence of the cavity mirrors is modeled using the term H_{Bire} , which introduces an energy splitting of $2\hbar\delta$ to the polarization modes. H_κ and H_γ are the non-Hermitian parts of the Hamiltonian. The term H_κ describes the dynamics of photons leaking out of the cavity, and can be described with collapse operators in the Lindblad treatment, e.g. $L_{rH} = \sqrt{2\kappa} |\uparrow, 0\rangle \langle \uparrow, rH|$ for a red and horizontally polarized photon. (In the following discussion, $|0\rangle$ represents the vacuum state in which no cavity photon is present in any mode.) Since the two projected states $|\uparrow, 0\rangle$ and $|\downarrow, 0\rangle$ are not included in the Hilbert space, this term can be treated as a non-hermitian term that represents population leakage from the metastable states $|\uparrow\rangle$ and $|\downarrow\rangle$. Similarly, $H_\gamma = -i\gamma_{xe} |e\rangle \langle e|$ describes a spontaneous emission from $|e\rangle$ to any other level $|x\rangle$ not resonant with the laser drives in the CART, including $|\uparrow\rangle$, $|\downarrow\rangle$ and other levels not explicitly considered. It is an effective description of the collapse operator $L_{xe} = \sqrt{2\gamma_{xe}} |x\rangle \langle e|$. Thus, the Hamiltonian has the form

$$H/\hbar = \begin{pmatrix} |i\rangle & |e\rangle & |\uparrow, rH\rangle & |\uparrow, rV\rangle & |\downarrow, bH\rangle & |\downarrow, bV\rangle \\ \frac{\delta_{\text{Stark}}}{2} & \frac{1}{2}\Omega(t) & & & & \\ \frac{1}{2}\Omega^*(t) & -\Delta_1 - i\gamma_{xe} & g_1 & & & \\ & g_1 & \delta_z - i\kappa & \delta_x - i\delta_y & & \\ & & \delta_x + i\delta_y & -\delta_z - i\kappa & & \\ & g_2 & & & \Delta_2 - \Delta_1 + \delta_z - i\kappa & \delta_x - i\delta_y \\ & & & & \delta_x + i\delta_y & \Delta_2 - \Delta_1 - \delta_z - i\kappa \end{pmatrix}, \quad (5)$$

where we denote the combined bichromatic laser drives as $\Omega(t) = \Omega_1 + \Omega_2 e^{i(\Delta_2 - \Delta_1)t}$, which creates a Stark shift of $\delta_{\text{Stark}} = \Omega_1^2/(4\Delta_1) + \Omega_2^2/(4\Delta_2)$. Here, Δ_j , Ω_j and g_j represent the laser detuning, drive Rabi frequency and atom-cavity coupling strength of the j^{th} Raman transition ($j \in \{1, 2\}$). The birefringence term $(\delta_x, \delta_y, \delta_z) = \delta \vec{e}_\delta$ are the components of the Stokes vector on the Poincaré sphere, with \vec{e}_δ describing the orientation of the two or-

thogonal cavity eigenmodes [46], and the magnitude δ being half the frequency splitting between them.

The collapse operators L_j used in the Lindblad equation is:

$$L_{ie} = \sqrt{2\gamma_{ie}} |i\rangle \langle e|. \quad (6)$$

L_{ie} describes the spontaneous emission from $|e\rangle$ back to $|i\rangle$. This collapse event is specially treated because

population driven off-resonantly from $|i\rangle$ to $|e\rangle$ that leaks back to $|i\rangle$ will remain in the subspace addressed by the laser drives, possibly resulting in emission of a delayed photon. This re-excitation process contributes to part of the fidelity loss, and will be elaborated on later in this section. In contrast, collapse events from L_{xe} do not result in the emission of cavity photons. Consequently, decay to these levels implies failure to generate a photon in the cavity mode. While such events reduce the REG rate, they do not directly affect the fidelity of heralded entanglement.

In order to find the atom-photon density matrix, we adopt the approach of [26] as follows: the eventual detection of a photon necessary for a heralding event can only occur if a collapse event L_{xe} has not occurred. Collapse events L_{ie} lead to a mixing of the temporal Hilbert space of the emitted photon. As such, we first seek to describe the state $|\phi\rangle$ of a pure photon that is extracted from the cavity with no collapse events during its evolution. We call this the "pure branch". Later, in Section III D, we will explicitly consider the impact of collapse events L_{ie} on the fidelity of the atom-atom entanglement scheme. The pure branch density matrix $\rho_0 = |\phi\rangle\langle\phi|$ can be found from Eq. 3 by removal of terms of the form $L_j\rho L_j^\dagger$:

$$\begin{aligned}\dot{\rho}_0 &= -\frac{i}{\hbar} (H\rho_0 - \rho_0 H^\dagger) - \sum_j \frac{1}{2} \{L_j^\dagger L_j, \rho_0\} \\ &= -\frac{i}{\hbar} (H_{\text{eff}}\rho_0 - \rho_0 H_{\text{eff}}^\dagger),\end{aligned}\quad (7)$$

where

$$H_{\text{eff}} = H - \sum_j \frac{i}{2} L_j^\dagger L_j. \quad (8)$$

In this case we can calculate the pure evolution of the photon by applying the Schrödinger equation to our non-Hermitian effective Hamiltonian:

$$|\dot{\phi}\rangle = -\frac{i}{\hbar} H_{\text{eff}} |\phi\rangle. \quad (9)$$

The leakage of photon can be described using creation operators of cavity photons and leaked photons defined by $a^\dagger(t) = \sqrt{2\kappa} a_{\text{cav}}^\dagger(t)$ [47].

Now we consider the output state of the photon from the cavity. For notational brevity, we make the choice to consider a red and horizontally polarized photon. The wave function of the output photon is

$$|\phi_{rH}^{\text{out}}\rangle = \sqrt{2\kappa} \int \langle \uparrow, rH | \phi(t) \rangle a_{rH}^\dagger(t) |0\rangle dt. \quad (10)$$

For simplicity we write it as

$$|\phi_{rH}^{\text{out}}\rangle = \int \varphi_{rH}(t) a_{rH}^\dagger |0\rangle dt = \tilde{a}_{rH}^\dagger |0\rangle, \quad (11)$$

where $\varphi_{rH}(t) = \sqrt{2\kappa} \langle \uparrow, rH | \phi(t) \rangle$. The derivation is analogous to that for other frequencies and polarizations. Fi-

nally, the atom-photon state can be written as:

$$|\phi\rangle_{\text{a-p}} = |\uparrow\rangle (\tilde{a}_{rH}^\dagger + \tilde{a}_{rV}^\dagger) |0\rangle + |\downarrow\rangle (\tilde{a}_{bH}^\dagger + \tilde{a}_{bV}^\dagger) |0\rangle, \quad (12)$$

which exhibits entanglement between the atomic qubit $|\uparrow\rangle, |\downarrow\rangle$ and the photonic qubit $|r\rangle, |b\rangle$.

B. Atom-atom entanglement

As shown in Fig. 1 (c), after the entangled atom-photon pairs are generated, the photons that leak out of the cavities are guided into optical fibers to the two input ports of a 50:50 beam splitter, and the photonic states are measured after each output port.

The full two-node quantum state immediately before interference on the beam splitter can be written as the tensor product of two single-node systems, as described in Eq. 12:

$$\begin{aligned}|\Phi\rangle &= (|\uparrow\rangle (\tilde{a}_{ArH}^\dagger + \tilde{a}_{ArV}^\dagger) + |\downarrow\rangle (\tilde{a}_{AbH}^\dagger + \tilde{a}_{AbV}^\dagger)) \\ &\otimes (|\uparrow\rangle (\tilde{b}_{BrH}^\dagger + \tilde{b}_{BrV}^\dagger) + |\downarrow\rangle (\tilde{b}_{BbH}^\dagger + \tilde{b}_{BbV}^\dagger)) |0\rangle,\end{aligned}\quad (13)$$

where the subscripts A and B refer to nodes A and B. We then apply the beam splitter transformation in Eq. 1, which gives the following output state:

$$\begin{aligned}|\Phi\rangle &= (|\uparrow\rangle (\tilde{c}_{ArH}^\dagger - \tilde{d}_{ArH}^\dagger + \tilde{c}_{ArV}^\dagger - \tilde{d}_{ArV}^\dagger) \\ &+ |\downarrow\rangle (\tilde{c}_{AbH}^\dagger - \tilde{d}_{AbH}^\dagger + \tilde{c}_{AbV}^\dagger - \tilde{d}_{AbV}^\dagger)) \\ &\otimes (|\uparrow\rangle (\tilde{c}_{BrH}^\dagger + \tilde{d}_{BrH}^\dagger + \tilde{c}_{BrV}^\dagger + \tilde{d}_{BrV}^\dagger) \\ &+ |\downarrow\rangle (\tilde{c}_{BbH}^\dagger + \tilde{d}_{BbH}^\dagger + \tilde{c}_{BbV}^\dagger + \tilde{d}_{BbV}^\dagger)) |0\rangle.\end{aligned}\quad (14)$$

Here, we again drop the explicit time dependence notation for simplicity. For example, the creation operators in the output ports are given by $\tilde{c}_{ArH}^\dagger = \int \varphi_{ArH}(t) c_{rH}^\dagger(t) dt$, for a red and horizontally polarized photon generated from node A.

We consider coincidence events with one red and one blue photon each detected in port \mathbf{c} using detection scheme (3) that ideally herald the atom-atom state $|\Psi^+\rangle = (|\uparrow\downarrow\rangle + |\downarrow\uparrow\rangle) / \sqrt{2}$. By applying its corresponding projection operator

$$P_{cc}^{\text{freq}}(t_r, t_b) = \sum_{x,y=H,V} c_{rx}(t_r)^\dagger c_{by}(t_b)^\dagger |0\rangle\langle 0| c_{rx}(t_r) c_{by}(t_b) \quad (15)$$

the projected state is given by

$$\begin{aligned} |\Phi_{cc}^{\text{freq}}\rangle &= P_{cc}^{\text{freq}} |\Phi\rangle \\ &= \sum_{x,y=H,V} \left[|\uparrow\downarrow\rangle \varphi_{Arx}(t_r) \varphi_{Bby}(t_b) \right. \\ &\quad \left. + |\downarrow\uparrow\rangle \varphi_{Aby}(t_b) \varphi_{Brx}(t_r) \right] c_{rx}^\dagger(t_r) c_{by}^\dagger(t_b) |0\rangle. \end{aligned} \quad (16)$$

After tracing out the photon states from Eq. 16, the atom-atom state takes the following form:

$$\rho_{cc}^{\text{freq}}(t_r, t_b) = \text{Tr}_p |\Phi_{cc}^{\text{freq}}\rangle \langle \Phi_{cc}^{\text{freq}}| = \sum_{x,y=H,V} |\Psi_{xy}\rangle \langle \Psi_{xy}|, \quad (17)$$

where

$$|\Psi_{xy}\rangle = |\uparrow\downarrow\rangle \varphi_{Arx}(t_r) \varphi_{Bby}(t_b) + |\downarrow\uparrow\rangle \varphi_{Aby}(t_b) \varphi_{Brx}(t_r). \quad (18)$$

Similarly, we derive the atom-atom entangled state for polarization encoding:

$$\begin{aligned} |\Psi_{cc}^{\text{pol}}(t_H, t_V)\rangle &= |\uparrow\uparrow\rangle \left(\varphi_{AHH}(t_H) \varphi_{BHV}(t_V) + \varphi_{AHV}(t_V) \varphi_{BHH}(t_H) \right) \\ &+ |\uparrow\downarrow\rangle \left(\varphi_{AHH}(t_H) \varphi_{BVV}(t_V) + \varphi_{AHV}(t_V) \varphi_{BVH}(t_H) \right) \\ &+ |\downarrow\uparrow\rangle \left(\varphi_{AVH}(t_H) \varphi_{BHV}(t_V) + \varphi_{AVV}(t_V) \varphi_{BHH}(t_H) \right) \\ &+ |\downarrow\downarrow\rangle \left(\varphi_{AVH}(t_H) \varphi_{BVV}(t_V) + \varphi_{AVV}(t_V) \varphi_{BVH}(t_H) \right), \end{aligned} \quad (19)$$

where the indices are arranged such that AHV stands for a photon from node A with initial horizontal polarization and rotated to vertical under birefringence. While the measurement is performed on the actual polarization, represented by the third index, the second index is still tracked because it indicates the ion state to which the photon is entangled. To understand Eq. 19, we examine the first term proportional to $|\uparrow\uparrow\rangle$. This term shows that if the photon from node B (A) was initially horizontal and was rotated to vertical under birefringence, this photon can be detected along with one horizontal photon from node A (B) that was not rotated under birefringence, and still register as a coincidence event with both detections on path c . Similarly, a $V \rightarrow H$ rotation from either node may introduce an admixture of $|\downarrow\downarrow\rangle$. This reduces the overlap with the desired asymmetric Bell state.

By comparing this to Eq. 18, we can see the advantage of frequency encoding. In the ideal case where wavefunctions from both nodes for the same frequency are identical (e.g., $\varphi_{Arx}(t_r) = \varphi_{Brx}(t_r) = \varphi_{rx}(t_r)$), the frequency encoded entangled state in Eq. 17 can be simplified to $|\Psi_{xy}\rangle = \varphi_{rx}(t_r) \varphi_{by}(t_b) (|\uparrow\downarrow\rangle + |\downarrow\uparrow\rangle)$, corresponding to an ideal Bell state with unity fidelity. In polarization encoding, the heralded state is still not ideal under this assumption, due to the aforementioned admixtures of

$|\uparrow\uparrow\rangle$ and $|\downarrow\downarrow\rangle$ in Eq. 19. In the no-birefringence limit, $\varphi_{HV}(t) = \varphi_{VH}(t) = 0$, the atom-atom entangled state is again proportional to $|\uparrow\downarrow\rangle + |\downarrow\uparrow\rangle$, as in the case for frequency encoding.

C. Entanglement Fidelity

Using the atom-atom entangled state derived from Eq. 17, the probability distribution of coincidence events where the photon pairs are detected at times (t_r, t_b) , can be calculated from the norm of the projected state:

$$\begin{aligned} p(t_r, t_b) &= \sum_{x,y=H,V} |\varphi_{Arx}(t_r) \varphi_{Bby}(t_b)|^2 \\ &\quad + |\varphi_{Aby}(t_b) \varphi_{Brx}(t_r)|^2. \end{aligned} \quad (20)$$

The corresponding atom-atom entanglement fidelity to the asymmetric Bell state is:

$$\begin{aligned} F(t_r, t_b) &= \frac{1}{2p(t_r, t_b)} \sum_{x,y=H,V} \left(|\varphi_{Arx}(t_r) \varphi_{Bby}(t_b)| \right. \\ &\quad \left. + |\varphi_{Aby}(t_b) \varphi_{Brx}(t_r)| \right)^2, \end{aligned} \quad (21)$$

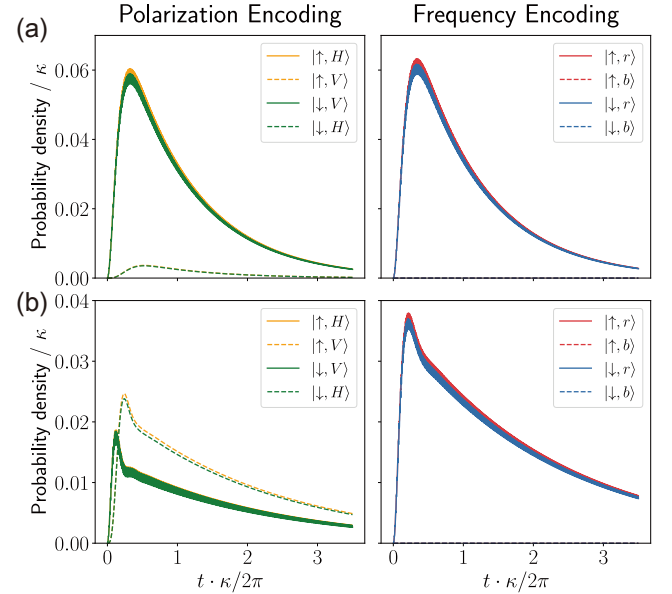


FIG. 2. Probability density of atom-photon correlation outcomes based on the polarization and frequency encoding schemes. (a) and (b) compare the wavepackets under different birefringence magnitudes: (a) $\delta = 0.3\kappa$ and (b) $\delta = 2\kappa$. Photons encoded by polarization (left) are represented by orange and green lines, while photons encoded by frequency (right) are represented by blue and red lines. The solid lines denote the probability density associated with the expected entangled atom-photon correlations, whereas the dashed lines denote the probability density of the incorrect correlations due to birefringence. The polarization degree of freedom is traced out for the frequency encoded case.

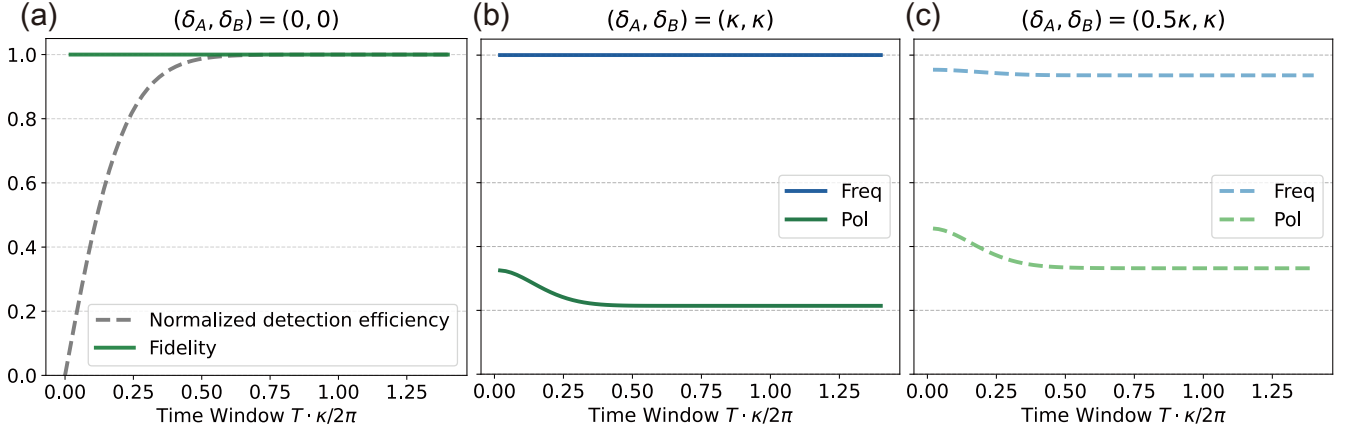


FIG. 3. Detection efficiency and atom-atom fidelity as a function of coincidence window length under different encoding schemes. The same cavity parameters are used for both frequency and polarization encoding schemes. (a) Detection efficiency and fidelity in the absence of birefringence. Both encoding schemes give unity fidelity. (b) and (c): Atom-atom fidelity under the same ((b)) and different ((c)) birefringence magnitude between the two nodes with frequency and polarization encoding.

where we have chosen the relative phase of the Bell state to maximize the overlap with ρ_{cc}^{freq} .

Note that if we use the detection scheme (2) shown in Fig. 1(c), photons with rotated polarization ($|V\rangle$ here) will be rejected by a PBS before being detected. In this case the summation in Eq. 20 and Eq. 21 can be removed by taking x, y as H . The fidelity will be slightly increased at the cost entanglement generation rate. In the remainder of this paper, we will use the detection scheme (3) as the default, where polarization is not filtered.

D. Re-excitation

In Section III A we derived the pure branch of the photon's evolution where no re-excitation events occur. However, Eq. 21 does not capture the effect of re-excitation errors from collapse events L_{ie} on the temporal purity of the cavity-emitted photons. In this section we extend our model to account for re-excitation, as this process is one of the most detrimental fidelity-reducing effects for remote entanglement generation (REG) in many atom-cavity systems [26, 48, 49].

Re-excitation events affect the REG fidelity by introducing mixing of the photonic wavepacket in the temporal Hilbert space. In the transition scheme shown in Fig. 1(a), the excited state $|e\rangle$ will typically have a lifetime on the order of nanoseconds, which is much shorter than the Raman pulse [48]. Decay from $|e\rangle$ to states other than the initial state $|i\rangle$ reduces the number of successful attempts, but because this process does not produce a photon in the cavity mode, it does not reduce the atom-atom entanglement fidelity. However, decay from $|e\rangle$ to $|i\rangle$ can still result in subsequent production of a photon in the cavity mode. This can be seen as an incoherent process that results in mixing of the photon's state in the temporal Hilbert space, diminishing the REG fidelity

[26, 49]. Modification to the Raman drive pulse, such as increasing of the detuning and pulse shaping [50], and careful choice of atomic level scheme [48, 51] can mitigate the effects of re-excitation errors.

To extend our model to account for re-excitation errors, we consider the photon emission time s to be a random variable with probability distribution $P(s)$. Then we may write the density matrix $\rho_{\text{re-ex}}$ as an integral of pure branch evolution density matrices $|\phi(t-s)\rangle\langle\phi(t-s)|$, weighted by the probability distribution for an event L_{ie} to occur:

$$\rho_{\text{re-ex}}(t) = \int P(s) |\phi(t-s)\rangle\langle\phi(t-s)| ds. \quad (22)$$

Here, $|\phi(t)\rangle$ is the pure photon state from (9), and $P(s)$ is given by

$$P(s) = \delta(s) + \langle e | \rho(s) | e \rangle, \quad (23)$$

where the additional delta function $\delta(s)$ centered at time $s = 0$ accounts for the initial pure branch where no collapse events occur. $\rho(s)$ is the mixed branch density matrix from Eq. 3.

Similar to Eq. 20, we can derive the final detection probability:

$$p(t_r, t_b) = \int P_A(s_A) P_B(s_B) ds_A ds_B \times \sum_{x,y=H,V} |\varphi_{Arx}(t_r - s_A) \varphi_{Bby}(t_b - s_B)|^2 + |\varphi_{Ary}(t_b - s_A) \varphi_{Brx}(t_r - s_B)|^2. \quad (24)$$

Finally, the atom-atom entanglement fidelity considering

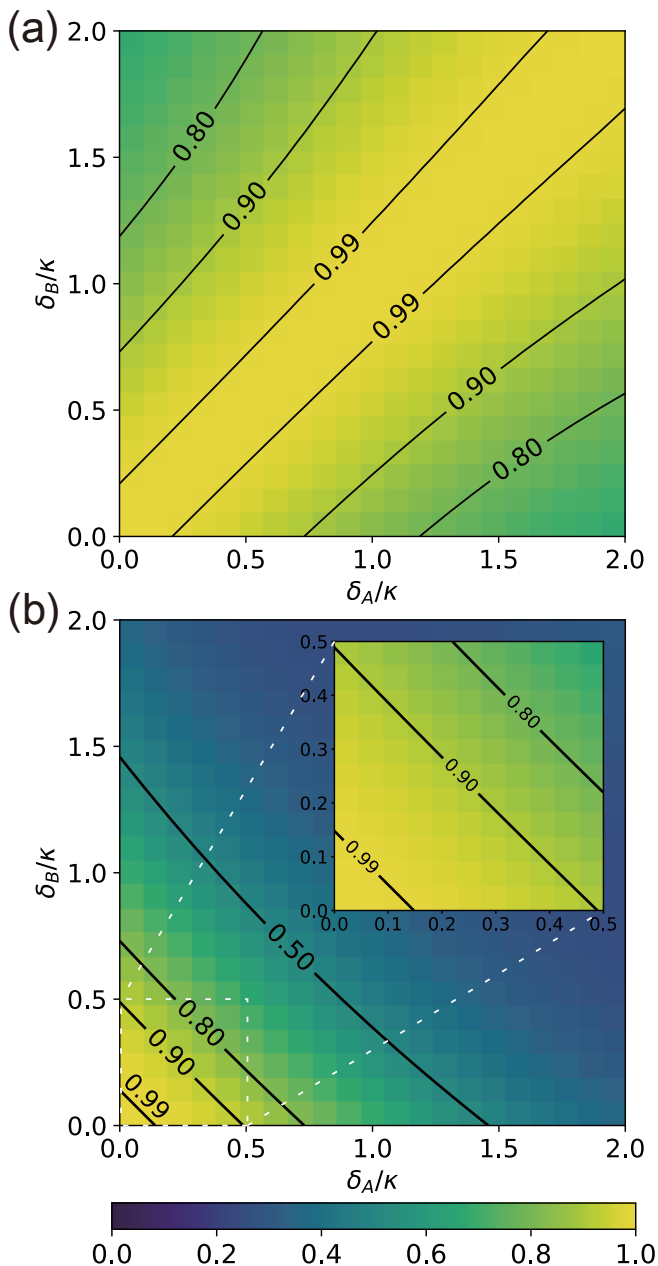


FIG. 4. Atom-atom fidelity versus birefringence magnitude at each node, using (a) frequency encoding and (b) polarization encoding. To demonstrate the effect of birefringence on the fidelity, results are derived from simulations with otherwise identical parameters and no re-excitation.

the re-excitation errors is given by

$$F(t_r, t_b) = \frac{1}{2p(t_r, t_b)} \int P_A(s_A) P_B(s_B) ds_A ds_B \times \sum_{x,y=H,V} \left(|\varphi_{Arx}(t_r - s_A) \varphi_{Bby}(t_b - s_B)| + |\varphi_{Aby}(t_b - s_A) \varphi_{Brx}(t_r - s_B)| \right)^2. \quad (25)$$

IV. NUMERICAL RESULTS

Due to the complexity of the Hamiltonian in Eq. 5, an analytical solution is not feasible. We conducted further numerical simulation on the CART and heralded entanglement based on two-photon interference. In this section we provide an overview of our simulation based on the model described in Section III. The advantages of the frequency encoding scheme are demonstrated by comparing entanglement fidelity under frequency encoding with that of the traditional polarization encoding scheme. Our results show that frequency encoding is robust against birefringence, whereas entanglement fidelity in polarization encoding deteriorates significantly when birefringence reaches the same order as the cavity decay rate κ .

For simplicity and to demonstrate the effect of birefringence, here we discard re-excitation events and assume that all other cavity parameters are identical for both nodes, so that any possible reduction in fidelity is caused by birefringence. The cavity eigenmodes are chosen as $(|H\rangle \pm |V\rangle)/\sqrt{2}$, corresponding to a Hamiltonian $H_{\text{Bire}} = \hbar\delta\sigma_x$. This choice maximizes rotation of the initial polarization, and results in the largest fidelity loss [45]. We first conduct simulations on the atom-photon output states. Fig. 2 shows some typical shape of photonic wavepackets generated from Hamiltonian in Eq. 5. The plotted curves show the emission probability of different atom-photon states measured at the output port as a function of time. The wavepackets are extracted from the pure state density matrix, which evolves following the regular Lindblad equation (Eq. 3). The Rabi frequencies are adjusted such that the photonic wavepackets of the two desired output states are well overlapped for maximal fidelity. Fig. 2(a) shows the wavepackets under small birefringence $\delta = 0.3\kappa$. For polarization-encoded photons, a fraction of each branch is rotated to its orthogonal polarization state, and the wavepacket is also balanced between two rotated components. In the case of frequency encoding, although similar polarization rotation occurs, the frequency is unchanged and the photonic qubit is always correlated with the correct atomic state. Under a larger birefringence $\delta = 2\kappa$, as shown in Fig. 2(b), the birefringent component is comparable to the non-birefringent component in polarization encoding. For frequency encoding, the wavepackets maintain similar shape with little influence from birefringence.

We then simulate atom-atom entanglement fidelity after two-photon interference. Fig. 3(a) shows the fidelity and efficiency as a function of coincidence window T in the absence of birefringence. Here, the coincidence window T represents the maximum allowed detection time difference for blue and red photons, $|t_r - t_b|$. For each T , the fidelity is averaged within the range $|t_r - t_b| \leq T$. Since re-excitation is ignored and both nodes are considered identical, the fidelity is always one, while the collection efficiency grows asymptotically, and is normalized such that it approaches one when T is much larger than

| Ion species | l/mm | R_c/mm | \mathcal{F} | FSR | g_1 | g_2 | κ | Ω_1 | Ω_2 | Δ_1, Δ_2 | γ_{ie} | γ_{xe} | δ |
|---------------------|---------------|-----------------|-----------------|---------------------|-------|-------|----------|------------|------------|----------------------|--------------------|---------------|-------------|
| $^{40}\text{Ca}^+$ | 0.493 | 0.493 | 5×10^4 | 304×10^3 | 9.36 | 8.89 | 6 | 38 | 40 | 400 | $10.78 \times 1/3$ | 7.92 | 0.5κ |
| $^{225}\text{Ra}^+$ | 10.8 | 10.8 | 5×10^4 | 13.84×10^3 | 1.01 | 1.01 | 0.28 | 40 | 40 | 400 | $1.69 \times 1/3$ | 9.00 | 0.5κ |

TABLE I. The parameters used for simulation. Values in columns \mathcal{F} , FSR, g_1 , g_2 , κ , Ω_1 , Ω_2 , Δ_1, Δ_2 , γ_{ie} and γ_{xe} are given in the unit of $2\pi \cdot \text{MHz}$. $\Omega_{1,2}$ and $\Delta_{1,2}$ represent the Rabi frequency and detuning for the two Raman drive lasers. γ_{ie} is the spontaneous emission rate from $|e\rangle$ back to $|i\rangle$, and γ_{xe} is the total spontaneous emission rate from $|e\rangle$ to all other levels. The atom-cavity coupling strength g_1 and g_2 for the two CARTs and the cavity decay rate κ are calculated according to cavity parameters: cavity length l , mirror radius of curvature R_c and finesse \mathcal{F} . For $^{225}\text{Ra}^+$ ion, l is designed such that the cavity FSR matches half the frequency difference between $|S_{1/2}, F=0, m_F=0\rangle$ and $|S_{1/2}, F=1, m_F=0\rangle$.

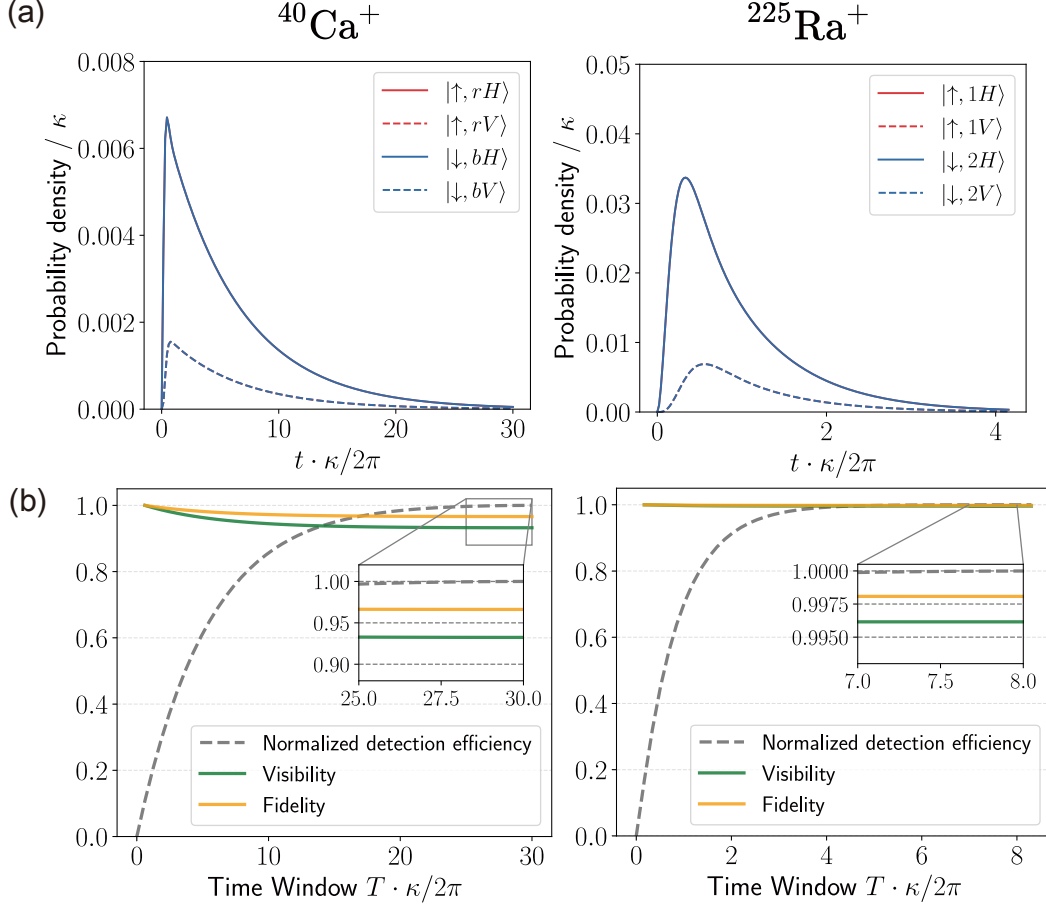


FIG. 6. (a) Atom-photon state at the cavity output of the frequency encoding scheme using $^{40}\text{Ca}^+$ and $^{225}\text{Ra}^+$ scheme. The blue and red curves represent photons of different frequency states, which overlap and are not distinguishable in the figure. (b) Detection efficiency, visibility of two-photon inference, and atom-atom fidelity under of the two use cases. Identical parameter settings are used for both nodes, and re-excitation process is considered. Insets show the asymptotic limit at long coincidence window.

effect while maintaining similar collection efficiency for pure photons, a large atom-cavity coupling strength g can limit population accumulation in the excited state. With these considerations, we model a fiber Fabry-Pérot cavity with a Finesse of $\mathcal{F} = 5 \times 10^4$, cavity length $l = 0.493 \text{ mm}$ and mirror radius of curvature $R_c = 0.493 \text{ mm}$. This gives a beam waist of $w = (8.24, 8.18) \mu\text{m}$, and $g/(2\pi) = -(14.8 \times \sqrt{10}/5, 15.4 \times \sqrt{3}/3) \text{ MHz}$ for the 866 nm and 854 nm transitions, respectively. The second operands come from the Clebsch-Gordan coefficients. We also set

the birefringence magnitude to be $\delta = 0.5\kappa$ and the cavity eigenbasis to be $(|H\rangle \pm |V\rangle)/\sqrt{2}$.

The simulation results are shown in Fig. 6. Assuming a large cavity decay $\kappa/(2\pi) = 6 \text{ MHz}$, the wavepacket shape is dominated by the Rabi frequency of the driving light. For small coincidence windows, the windowed fidelity starts at 100%, decreasing for a larger time window and eventually saturating at 96.6% for longer ones, limited by re-excitation errors.

B. Qubits with hyperfine splitting

Frequency-encoded photons can also be generated using atoms with hyperfine structure. We consider an experimental scheme utilizing the ground state of $^{225}\text{Ra}^+$ with nuclear spin $I = 1/2$ that has a large hyperfine splitting and a photonic qubit at 468 nm. The atom is initially prepared at $|i\rangle = |D_{3/2}, F = 1, m_F = 0\rangle$ and driven to $|\uparrow\rangle = |S_{1/2}, F = 1, m_F = 0\rangle$ and $|\downarrow\rangle = |S_{1/2}, F = 0, m_F = 0\rangle$ respectively via CART, mediated by excited state $|e\rangle = |P_{1/2}, F = 1, m_F = -1\rangle$. The two possible photonic states emitted in this process each have a wavelength near 468 nm with frequency difference 27.68 GHz [54].

One advantage of using $^{225}\text{Ra}^+$ is its lower decay rate back to the initial state $\gamma_{ie}/(2\pi) = 1.69 \times 1/3$ MHz, leading to much lower re-excitation infidelity than in the $^{40}\text{Ca}^+$ scheme. However, due to the small frequency difference of just 27.68 GHz, the cavity FSR needs to be such that the cavity supports both frequency modes. To meet this demand, we model a confocal cavity with a length of $l = 10.8$ mm and mirror radius of curvature $R_c = 10.8$ mm. The beam waist in this case is $w = 28$ μm , and $g/(2\pi) = 1.75 \times 1/\sqrt{3}$ MHz. We choose for both cavities the same birefringence ($\delta = 0.5\kappa$) and the cavity eigenmode ($(|H\rangle \pm |V\rangle)/\sqrt{2}$) as above. The simulation results are shown in Fig. 6. The windowed fidelity starts at 100% and decreases to 99.8% asymptotically for an arbitrarily long coincidence window.

VI. CONCLUSION

We have presented a novel experimental scheme for a cavity-based quantum network using frequency-encoded photonic qubits. Compared to polarization encoding, this scheme is less sensitive to cavity birefringence, with its only contribution to infidelity originating from the reduction in indistinguishability resulting from differences in birefringence between the two nodes.

We performed a detailed numerical analysis comparing frequency and polarization encoding to validate the effectiveness of our proposed scheme. This analysis includes the temporal emission probability of photonic states, two-photon interference visibility, and an evaluation of the robustness in entanglement fidelity to cavity bire-

fringence. Furthermore, we discuss two implementations that show that even with substantial common birefringence [31] in the two nodes $\delta_1 = \delta_2 = 0.5\kappa$, fidelities of 96.6% for $^{40}\text{Ca}^+$ and 99.8% for $^{225}\text{Ra}^+$ can be achieved.

Frequency encoding in a cavity-based quantum network still requires further experimental validation, and we identify several implementation challenges. Firstly, a proper detection and manipulation protocol of frequency-bin photons [55] should be carefully selected or developed to achieve ideal separation between bichromatic photons. Secondly, compensation for fiber dispersion may be necessary; otherwise, temporal distinguishability may be introduced if the difference in arrival times of the two colors of photon reaches the scale of their bandwidth. These effects rely heavily on the chosen qubit frequency, as a larger difference in frequency might simplify detection, but introduce more dispersion. Fiber-induced polarization drift should also be actively stabilized in all encoding schemes [33, 35], including frequency encoding. Additionally, frequency encoding does not guarantee high fidelity when the birefringence in both nodes is not identical. These errors can be further mitigated by optimizing the Raman laser and cavity parameters at the two nodes for maximal indistinguishability, including laser detuning, laser drive Rabi frequency, atom-cavity coupling strength, cavity decay rate, etc.

Our findings pave the way for a more robust design of cavity-based quantum networks, offering an alternate path towards achieving high-fidelity, scalable quantum entanglement over long distances. Together with experimental realization, our scheme can find wide application in quantum key distribution, quantum enhanced sensing, and distributed quantum computing.

VII. ACKNOWLEDGMENTS

We thank Wance Wang, Ezra Kassa and Yiheng Lin for their helpful discussion. Q.W. and H.H. acknowledge funding by the U.S. Department of Energy, Office of Science, Office of Basic Energy Sciences under Awards No. DE-SC0023277. This work was supported by the Office of Advanced Scientific Computing Research (ASCR), Office of Science, U.S. Department of Energy, under Contract No. DE-AC02-05CH11231. The research was executed under the Quantum Internet to Accelerate Scientific Discovery ASCR Research Program funded through Berkeley Lab FWP FP00013429.

-
- [1] M. DeCross, R. Haghshenas, M. Liu, Y. Alexeev, C. H. Baldwin, J. P. Bartolotta, M. Bohn, E. Chertkov, J. Colina, D. DeVento, *et al.*, The computational power of random quantum circuits in arbitrary geometries, arXiv preprint arXiv:2406.02501 (2024).
- [2] D. Bluvstein, S. J. Evered, A. A. Geim, S. H. Li, H. Zhou, T. Manovitz, S. Ebadi, M. Cain, M. Kalinowski,

- D. Hangleiter, *et al.*, Logical quantum processor based on reconfigurable atom arrays, *Nature* **626**, 58 (2024).
- [3] A. W. Young, W. J. Eckner, W. R. Milner, D. Kedar, M. A. Norcia, E. Oelker, N. Schine, J. Ye, and A. M. Kaufman, Half-minute-scale atomic coherence and high relative stability in a tweezer clock, *Nature* **588**, 408 (2020).

- [4] J. Franke, S. R. Muleady, R. Kaubruegger, F. Kranzl, R. Blatt, A. M. Rey, M. K. Joshi, and C. F. Roos, Quantum-enhanced sensing on optical transitions through finite-range interactions, *Nature* **621**, 740 (2023).
- [5] S.-A. Guo, Y.-K. Wu, J. Ye, L. Zhang, W.-Q. Lian, R. Yao, Y. Wang, R.-Y. Yan, Y.-J. Yi, Y.-L. Xu, *et al.*, A site-resolved two-dimensional quantum simulator with hundreds of trapped ions, *Nature* **630**, 613 (2024).
- [6] S. Ebadi, T. T. Wang, H. Levine, A. Keesling, G. Semeghini, A. Omran, D. Bluvstein, R. Samajdar, H. Pichler, W. W. Ho, *et al.*, Quantum phases of matter on a 256-atom programmable quantum simulator, *Nature* **595**, 227 (2021).
- [7] C. Hempel, C. Maier, J. Romero, J. McClean, T. Monz, H. Shen, P. Jurcevic, B. P. Lanyon, P. Love, R. Babbush, *et al.*, Quantum chemistry calculations on a trapped-ion quantum simulator, *Physical Review X* **8**, 031022 (2018).
- [8] H. J. Manetsch, G. Nomura, E. Bataille, K. H. Leung, X. Lv, and M. Endres, A tweezer array with 6100 highly coherent atomic qubits, arXiv preprint arXiv:2403.12021 (2024).
- [9] M. Malinowski, D. Allcock, and C. Ballance, How to wire a 1000-qubit trapped-ion quantum computer, *PRX Quantum* **4**, 040313 (2023).
- [10] H. J. Kimble, The quantum internet, *Nature* **453**, 1023 (2008).
- [11] S. Wehner, D. Elkouss, and R. Hanson, Quantum internet: A vision for the road ahead, *Science* **362**, 6412 (2018).
- [12] J. I. Cirac, A. Ekert, S. F. Huelga, and C. Macchiavello, Distributed quantum computation over noisy channels, *Physical Review A* **59**, 4249 (1999).
- [13] L. Jiang, J. M. Taylor, A. S. Sørensen, and M. D. Lukin, Distributed quantum computation based on small quantum registers, *Physical Review A—Atomic, Molecular, and Optical Physics* **76**, 062323 (2007).
- [14] D. Main, P. Drmota, D. Nadlinger, E. Ainley, A. Agrawal, B. Nichol, R. Srinivas, G. Araneda, and D. Lucas, Distributed quantum computing across an optical network link, *Nature*, 1 (2025).
- [15] D. Bouwmeester, J.-W. Pan, K. Mattle, M. Eibl, H. Weinfurter, and A. Zeilinger, Experimental quantum teleportation, *Nature* **390**, 575 (1997).
- [16] L.-M. Duan and H. Kimble, Efficient engineering of multiatom entanglement through single-photon detections, *Physical review letters* **90**, 253601 (2003).
- [17] C. Monroe, R. Raussendorf, A. Ruthven, K. R. Brown, P. Maunz, L.-M. Duan, and J. Kim, Large-scale modular quantum-computer architecture with atomic memory and photonic interconnects, *Physical Review A* **89**, 022317 (2014).
- [18] Y. Li and J. D. Thompson, High-rate and high-fidelity modular interconnects between neutral atom quantum processors, *PRX Quantum* **5**, 020363 (2024).
- [19] J. Sinclair, J. Ramette, B. Grinkemeyer, D. Bluvstein, M. Lukin, and V. Vuletić, Fault-tolerant optical interconnects for neutral-atom arrays, arXiv preprint arXiv:2408.08955 (2024).
- [20] L. Stephenson, D. Nadlinger, B. Nichol, S. An, P. Drmota, T. Ballance, K. Thirumalai, J. Goodwin, D. Lucas, and C. Ballance, High-rate, high-fidelity entanglement of qubits across an elementary quantum network, *Physical review letters* **124**, 110501 (2020).
- [21] J. O'Reilly, G. Toh, I. Goetting, S. Saha, M. Shalaev, A. L. Carter, A. Risinger, A. Kalakuntla, T. Li, A. Verma, *et al.*, Fast photon-mediated entanglement of continuously cooled trapped ions for quantum networking, *Physical Review Letters* **133**, 090802 (2024).
- [22] T. van Leent, M. Bock, F. Fertig, R. Garthoff, S. Eppelt, Y. Zhou, P. Malik, M. Seubert, T. Bauer, W. Rosenfeld, *et al.*, Entangling single atoms over 33 km telecom fibre, *Nature* **607**, 69 (2022).
- [23] A. Reiserer and G. Rempe, Cavity-based quantum networks with single atoms and optical photons, *Reviews of Modern Physics* **87**, 1379 (2015).
- [24] L. Hartung, M. Seubert, S. Welte, E. Distanto, and G. Rempe, A quantum-network register assembled with optical tweezers in an optical cavity, *Science* **385**, 179 (2024).
- [25] J. Schupp, V. Krcmarsky, V. Krutyanskiy, M. Meraner, T. E. Northup, and B. P. Lanyon, Interface between trapped-ion qubits and traveling photons with close-to-optimal efficiency, *PRX quantum* **2**, 020331 (2021).
- [26] V. Krutyanskiy, M. Galli, V. Krcmarsky, S. Baier, D. Fioretto, Y. Pu, A. Mazloom, P. Sekatski, M. Canteri, M. Teller, *et al.*, Entanglement of trapped-ion qubits separated by 230 meters, *Physical Review Letters* **130**, 050803 (2023).
- [27] D. Hunger, T. Steinmetz, Y. Colombe, C. Deutsch, T. W. Hänsch, and J. Reichel, A fiber fabry-perot cavity with high finesse, *New Journal of Physics* **12**, 065038 (2010).
- [28] R. Gehr, J. Volz, G. Dubois, T. Steinmetz, Y. Colombe, B. L. Lev, R. Long, J. Esteve, and J. Reichel, Cavity-based single atom preparation and high-fidelity hyperfine state readout, *Physical review letters* **104**, 203602 (2010).
- [29] H. Takahashi, E. Kassa, C. Christoforou, and M. Keller, Strong coupling of a single ion to an optical cavity, *Physical review letters* **124**, 013602 (2020).
- [30] M. Uphoff, M. Brekenfeld, G. Rempe, and S. Ritter, Frequency splitting of polarization eigenmodes in microscopic fabry-perot cavities, *New Journal of Physics* **17**, 013053 (2015).
- [31] H. Takahashi, J. Morphew, F. Oručević, A. Noguchi, E. Kassa, and M. Keller, Novel laser machining of optical fibers for long cavities with low birefringence, *Optics express* **22**, 31317 (2014).
- [32] S. Kucera, C. Haen, E. Arenskötter, T. Bauer, J. Meiers, M. Schäfer, R. Boland, M. Yahyapour, M. Lessing, R. Holzwarth, *et al.*, Demonstration of quantum network protocols over a 14-km urban fiber link, *npj Quantum Information* **10**, 88 (2024).
- [33] C. Knaut, A. Suleymanzade, Y.-C. Wei, D. Assumpcao, P.-J. Stas, Y. Huan, B. Machielse, E. Knall, M. Sutula, G. Baranes, *et al.*, Entanglement of nanophotonic quantum memory nodes in a telecom network, *Nature* **629**, 573 (2024).
- [34] S. Saha, M. Shalaev, J. O'Reilly, I. Goetting, G. Toh, A. Kalakuntla, Y. Yu, and C. Monroe, High-fidelity remote entanglement of trapped atoms mediated by time-bin photons, arXiv preprint arXiv:2406.01761 (2024).
- [35] M. T. Uysal, Ł. Dusanowski, H. Xu, S. P. Horvath, S. Ourari, R. J. Cava, N. P. de Leon, and J. D. Thompson, Spin-photon entanglement of a single Er^{3+} ion in the telecom band, arXiv preprint arXiv:2406.06515 (2024).
- [36] L. Li, X. Hu, Z. Jia, W. Huie, W. K. C. Sun, Y. Dong, J. P. Covey, *et al.*, Parallelized telecom quantum networking with a ytterbium-171 atom array, arXiv preprint

- arXiv:2502.17406 (2025).
- [37] P. Maunz, S. Olmschenk, D. Hayes, D. Matsukevich, L.-M. Duan, and C. Monroe, Heralded quantum gate between remote quantum memories, *Physical review letters* **102**, 250502 (2009).
- [38] S. C. Connell, J. Scarabel, E. M. Bridge, K. Shimizu, V. Blüms, M. Ghadimi, M. Lobino, and E. W. Streed, Ion–photonic frequency qubit correlations for quantum networks, *Journal of Physics B: Atomic, Molecular and Optical Physics* **54**, 175503 (2021).
- [39] A. Kuhn, M. Hennrich, and G. Rempe, Deterministic single-photon source for distributed quantum networking, *Physical review letters* **89**, 067901 (2002).
- [40] A. Stute, B. Casabone, P. Schindler, T. Monz, P. O. Schmidt, B. Brandstätter, T. E. Northup, and R. Blatt, Tunable ion–photon entanglement in an optical cavity, *Nature* **485**, 482 (2012).
- [41] C.-K. Hong, Z.-Y. Ou, and L. Mandel, Measurement of subpicosecond time intervals between two photons by interference, *Physical review letters* **59**, 2044 (1987).
- [42] T. Legero, T. Wilk, M. Hennrich, G. Rempe, and A. Kuhn, Quantum beat of two single photons, *Physical review letters* **93**, 070503 (2004).
- [43] L. Stephenson, *Entanglement between nodes of a quantum network* (University of Oxford (United Kingdom), 2020).
- [44] S. Garcia, F. Ferri, K. Ott, J. Reichel, and R. Long, Dual-wavelength fiber fabry-perot cavities with engineered birefringence, *Optics express* **26**, 22249 (2018).
- [45] E. Kassa, W. Hughes, S. Gao, and J. F. Goodwin, Effects of cavity birefringence in polarisation-encoded quantum networks, *New Journal of Physics* **25**, 013004 (2023).
- [46] T. D. Barrett, O. Barter, D. Stuart, B. Yuen, and A. Kuhn, Polarization oscillations in birefringent emitter-cavity systems, *Physical Review Letters* **122**, 083602 (2019).
- [47] H. Goto, S. Mizukami, Y. Tokunaga, and T. Aoki, Figure of merit for single-photon generation based on cavity quantum electrodynamics, *Physical Review A* **99**, 053843 (2019).
- [48] T. Walker, S. V. Kashanian, T. Ward, and M. Keller, Improving the indistinguishability of single photons from an ion-cavity system, *Physical Review A* **102**, 032616 (2020).
- [49] M. Meraner, A. Mazloom, V. Krutyanskiy, V. Krcmarsky, J. Schupp, D. Fioretto, P. Sekatski, T. Northup, N. Sangouard, and B. Lanyon, Indistinguishable photons from a trapped-ion quantum network node, *Physical Review A* **102**, 052614 (2020).
- [50] K. Tanji, H. Takahashi, W. Roga, and M. Takeoka, Rate-fidelity tradeoff in cavity-based remote entanglement generation, *Physical Review A* **110**, 042405 (2024).
- [51] S. Kikura, R. Asaoka, M. Koashi, and Y. Tokunaga, High-purity single-photon generation based on cavity qed, arXiv preprint arXiv:2403.00072 (2024).
- [52] P.-C. Lai, Y. Wang, J.-X. Shi, Z.-B. Cui, Z.-Q. Wang, S. Zhang, P.-Y. Liu, Z.-C. Tian, Y.-D. Sun, X.-Y. Chang, *et al.*, Realization of a crosstalk-free two-ion node for long-distance quantum networking, *Physical Review Letters* **134**, 070801 (2025).
- [53] M. Hettrich, T. Ruster, H. Kaufmann, C. Roos, C. Schmiegelow, F. Schmidt-Kaler, and U. Poschinger, Measurement of dipole matrix elements with a single trapped ion, *Physical review letters* **115**, 143003 (2015).
- [54] R. Ready, H. Li, S. Kofford, R. Kwapisz, H. Dan, A. Sawhney, M. Fan, C. Holliman, X. Shi, L. Sever-Walter, *et al.*, Laser cooling of radium-225 ions, arXiv preprint arXiv:2407.14721 (2024).
- [55] H.-H. Lu, E. M. Simmerman, P. Lougovski, A. M. Weiner, and J. M. Lukens, Fully arbitrary control of frequency-bin qubits, *Physical Review Letters* **125**, 120503 (2020).